EES Solar

PAPER

View Article Online
View Journal

Cite this: DOI: 10.1039/d5el00168d

Dual functions of the anchoring groups in self-assembled molecules as effective hole-selective contacts in inverted perovskite solar cells

Carlos E. Puerto Galvis, [a] José G. Sánchez, [a] Eugenia Martínez-Ferrero, [a] Wenhui Li *[a] and Emilio Palomares *[ab]

Self-assembled molecules (SAMs) have emerged as highly efficient hole-selective contacts in inverted perovskite solar cells (PSCs). Gaining insight into the role of individual molecular moieties is essential for the rational design of efficient SAMs. Herein, we systematically investigate four kinds of anchoring groups: carboxylic acid (–COOH), cyanoacetic acid (CN/COOH), phosphonic acid ($-PO(OH)_2$) and cyano/cyano (CN/CN) in the EADR03 molecular framework to elucidate their roles on interfacial charge transfer. Our findings indicate that either carboxylic, cyanoacetic or phosphonic acid effectively binds to ITO, forming an ultra-thin layer. Interestingly, these anchoring groups passivate the buried interface, inducing high-quality perovskite films. Among them, the phosphonic acid-based derivative gives the highest efficiencies among all the anchoring groups tested, enabling 24.0% efficiency for 1.55 eV bandgap perovskite. In this work, we have carried out microscopic, photoluminescence and X-ray photoelectron spectroscopy studies at the ITO/SAM/perovskite interface, complemented with kinetic characterization on devices, to understand the dual functions of the anchoring groups of SAMs at two different interfaces, opening the path for further improvement in the innovative design of efficient molecules.

Received 12th October 2025
Accepted 20th April 2026

DOI: 10.1039/d5el00168d

rsc.li/EESSolar

Broader context

Self-assembled molecules (SAMs) as hole-selective contacts have promoted the efficiency of perovskite solar cells (PSCs) to 27%, demonstrating their pivotal role in interfacial engineering. To surpass this milestone and approach the thermodynamic efficiency limit of PSCs, a deeper understanding is required on how SAMs induce interfacial binding chemistry and perovskite crystallization at the buried interface. The molecular design of SAMs, particularly the choice of anchoring group, plays a crucial yet often overlooked role in governing the quality of the overlying perovskite film and interfacial charge extraction. In this work, we systematically tailored the molecular chemistry of a benchmark SAM to reveal how different anchoring groups affect interfacial binding, crystal growth, and device performance. Our findings reveal that phosphonic acid anchoring groups promote the formation of high-quality and defect-suppressed perovskite films at the buried interface, enabling enhanced charge extraction and higher-performance inverted PSCs. These insights advance our molecular-level understanding of SAM-perovskite interactions and provide guidelines for designing SAMs to realize efficient, stable, and scalable perovskite photovoltaics.

Introduction

Self-assembled molecules (SAMs) have shown great potential when used as hole-selective contacts (HSCs) for high-performance inverted perovskite solar cells (PSCs), achieving power conversion efficiencies (PCE) of 27%.[1–6] SAMs as HSCs have the advantages of low material consumption, minimal parasitic absorption, reduced interfacial non-radiative recombination and enhanced device stability.[7–11] A SAM consists of three parts: anchoring group, spacer and functional group. Generally, the anchoring group of SAM allows for chemical bonding to the transparent conductive oxide substrates (tin-doped indium oxide, ITO and fluorine-doped tin oxide, FTO) to form an ultra-thin charge-selective contact. The spacer assists the self-assembly of the molecules and stabilizes the intramolecular charge. The functional group enriched with electron-donating moieties favor the hole transport.[7,12]

Currently, the high-performance inverted PSCs are based on the SAM with an anchoring group of carboxylic acid (–COOH), cyanoacetic acid (CN/COOH) or phosphonic acid ($-PO(OH)_2$).[2,4,13–15] Specifically, the carboxylic acid results in mono- or bidentate binding to ITO/FTO, whereas the phosphonic acid anchors as mono-, bi-, and tridentate binding modes to ITO/FTO.[16] Both anchoring groups strongly bind to the substrate to form a uniform SAM layer. In addition, the nitrile (–CN) group has been reported to passivate the perovskite to form high-quality films.[1,14] The reported SAMs bearing

[a]Institute of Chemical Research of Catalonia (ICIQ-CERCA), Avda. Països Catalans, 16, 43007 Tarragona, Spain. E-mail: wli@iciq.esepalomares@iciq.es
[b]Catalan Institution for Research and Advanced Studies (ICREA), 08010 Barcelona, Spain

phosphonic acid anchoring groups often exhibit higher efficiencies (summarized in Table S5); however, the underlying reason remains poorly understood, especially how the anchoring groups affect the crystal growth and crystallinity of perovskite film. Moreover, high efficiency SAM-based devices rely on additional surface passivation using ammonium salts, which may hide the intrinsic contribution of SAMs to perovskite crystallization and their passivation effect. Therefore, in this work, we have investigated the role of the anchoring groups to understand their impact on the device performance, without using additives for bulk and surface passivation.

Herein, we have systematically investigated four popular and efficient anchoring groups, namely –COOH, CN/COOH, –$PO(OH)_2$ and CN/CN, on the device performance by modifying the molecular framework of EADR03. This commercially available SAM has demonstrated excellent efficiency in p-i-n solar cells.[2] We found that carboxylic acid, cyanoacetic acid and phosphonic acid show strong binding effects with ITO. In addition, and more interestingly, the anchoring groups can also passivate the buried perovskite interface, as previously reported,[17] but with different effects. Specifically, the phosphonic acid anchoring groups passivate the buried interface and induce higher quality perovskite film when compared to the other three anchoring groups, leading to a PCE over 21% based on 1.61 eV bandgap and 24.0% for 1.55 eV bandgap triple cations PSC without using additional bulk and surface passivation molecules. Microscopy and spectroscopic studies have been carried out to study the interface, which has been complemented by X-ray photoelectron spectroscopy. Finally, kinetic characterization on devices has been done to achieve a more complete picture of the influence of the different anchoring groups in the charge transfer processes.

Results and discussion

Fig. 1a displays the molecular structure of the SAMs with different anchoring groups, including –COOH (EADR03, 4-(3,6-bis(2,4-dimethoxyphenyl)-9*H*-carbazol-9-yl)benzoic acid), CN/COOH (CP203, (E)-3-(4-(3,6-bis(2,4-dimethoxyphenyl)-9*H*-carbazol-9-yl)phenyl)-2-cyanoacrylic acid), –$PO(OH)_2$ (CP204, (4-(3,6-bis(2,4-dimethoxyphenyl)-9*H*-carbazol-9-yl)phenyl) phosphonic acid), and CN/CN (CP226, 2-(4-(3,6-bis(2,4-dimethoxyphenyl)-9*H*-carbazol-9-yl)benzylidene)malononitrile). The molecules' calculated electrostatic surface potentials (ESPs) point to the electron-withdrawing characteristics of the anchoring groups, which could anchor to the ITO surface and possibly interact with the perovskite film at the buried interface.[18] Moreover, the molecules show significant dipole moments (Fig. S1) which could modulate the work function of ITO.[19] We conducted X-ray photoelectron spectroscopy (XPS) to confirm the atomic bonds between different anchoring groups and ITO. The C 1s spectra (Fig. 1b) can be fitted to four peaks assigned to aromatic carbon C–C or C–H at 284.7 eV, carbazole moiety C–N at 285.3 eV, methoxy C–O–C at 286.5 eV and carboxylic acid O–C=O at 288.6 eV, respectively.[2,3] The ITO peak can also be fitted to adventitious C–C (or C–H), C–O and O–C=O carbon bonds due to the impurities of the ITO surface during the cleaning process. However, CP226 with CN/CN anchoring group shows the same carbon bonds as ITO, most probably due to the weak bonding of CN/CN with ITO. We analyzed the O 1s (Fig. 1c) and N 1s (Fig. S2) spectra. EADR03, CP203 and CP204 show the signal corresponding to C–O–In (or P–O–In) and C=O···In (or P=O···In) at 531.2 eV, and the reduced –OH content (Table S1) compared to bare ITO, indicating the practical bonding effect between –COOH/–$PO(OH)_2$ with ITO.[20] However, we cannot conclude that CP226 is bonded to ITO, confirming our hypothesis that only a few CP226 molecules are deposited onto the ITO surface due to the weak interaction between the CN/CN anchoring group and ITO.

The surface morphology and wettability were characterized by atomic force microscopy (AFM) and contact angle measurements on substrates of bare ITO and SAMs deposited on ITO (Fig. 2 and S3). The AFM results indicate that the SAMs conformally cover the surface of ITO. Moreover, the roughness mean square values (RMS) show similar values in all cases, pointing towards the formation of an ultra-thin layer. In addition, the water contact angles on bare ITO, EADR03, CP203, CP204 and CP226 are 25°, 60°, 61°, 63° and 36°, respectively. EADR03, CP203 and CP204 show similar wettability, as expected for molecules with similar functional groups. Meanwhile, the contact angle of CP226 is slightly higher than bare ITO's. These results suggest that –COOH, CN/COOH and –$PO(OH)_2$ anchoring groups strongly bond to ITO, forming a uniform layer. In contrast, the CN/CN anchoring group does not form strong bonds, resulting in poor SAM coverage of the ITO surface.

After confirming the bonding information of the SAMs deposited onto ITO, we used photoluminescence (PL) to analyze the charge recombination behavior at the buried interface based on the substrates of ITO/SAMs/perovskite ($Cs_{0.05}(FA_{0.85}MA_{0.15})_{0.95}Pb(I_{0.85}Br_{0.15})_3$). A 635 nm laser was excited from the ITO side, as shown in Fig. 3a. The perovskites deposited on EADR03, CP203 and CP204 have higher PL emission than the perovskites deposited on bare ITO and CP226. The increased emission is due to the passivation effect from the SAMs, which reduces the interfacial non-radiative recombination caused by defects.[3,21] Moreover, CP204, with the phosphonic acid anchoring group, has the highest emission intensity among all the SAMs, highlighting that the presence of phosphonic acid has a more effective passivation effect than carboxylic acid and cyanoacetic acid to grow high-quality perovskite crystals. The time-resolved photoluminescence (TrPL) further confirms that phosphonic acid, carboxylic acid and cyanoacetic acid can passivate the perovskite; significantly, the phosphonic acid induces the growth of high-quality perovskite film with the longest decay time (Fig. S4 and Table S2). We implemented a space charge limited current (SCLC) test *via* a hole-only configuration of ITO/SAMs/Perovskite/MoO_3/Au under dark conditions to evaluate the trap density (Fig. S5). The defect densities for EADR03, CP203 and CP204-based devices were calculated to be 4.42×10^{15} cm^{-3}, 5.89×10^{15} cm^{-3} and 2.39×10^{15} cm^{-3}, respectively, indicating that CP204 with phosphonic acid could more effectively passivate the defects in the SAM/perovskite contact interface.

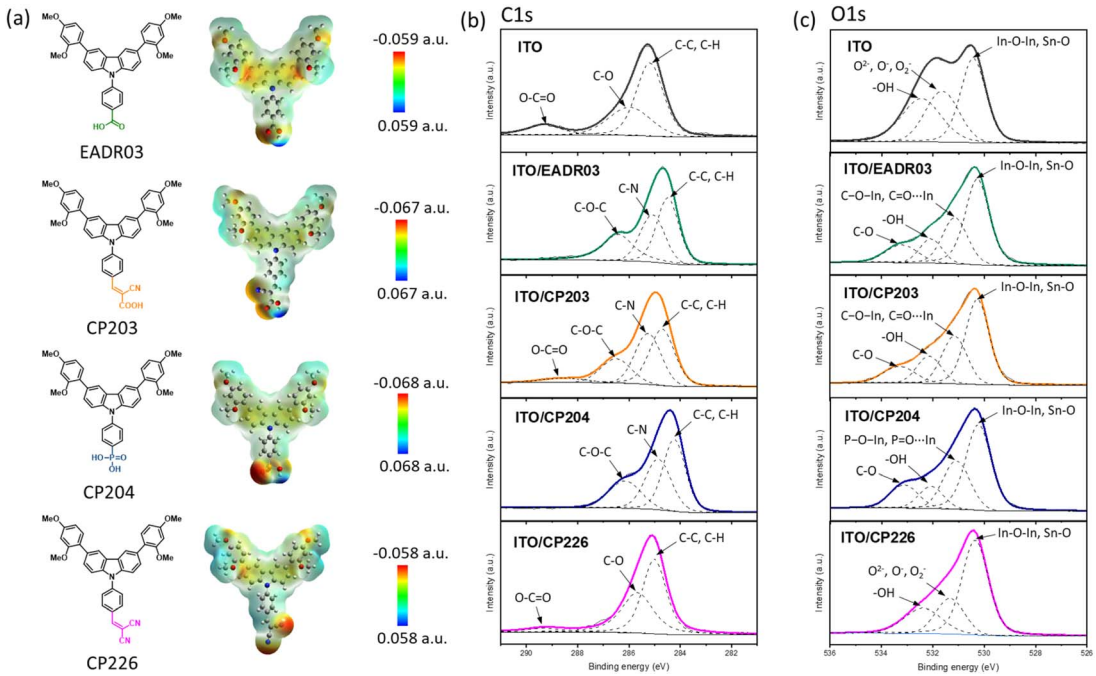

Fig. 1 (a) Chemical structure of the molecules (EADR03, CP203, CP204 and CP226) and the corresponding calculated electrostatic surface potentials (ESPs). High-resolution XPS survey spectra of the (b) C 1s region and (c) O 1s region of ITO, ITO/EADR03, ITO/CP203, ITO/CP204 and ITO/CP226.

We also performed the PL with the excitation from the ITO and perovskite sides to confirm the perovskite quality at the top surface and buried interface, respectively, as shown in Fig. 3a and b. The PL intensity of top perovskite surface deposited on EADR03, CP203 and CP204 decreases when compared to the corresponding PL intensity of the buried interfaces, while the PL intensity of perovskite deposited on bare ITO and CP226 is almost the same at the top surface and buried interface (Fig. S6), indicating that the anchoring groups can induce the formation of higher quality perovskite crystals at the buried interface than the top surface. Moreover, we conducted a high-resolution transmission electron microscope (TEM) analysis of the perovskite crystal quality at different film parts. We took ITO/CP203 with a cyanoacetic acid anchoring group and ITO/CP204 with a phosphonic acid anchoring group as examples to study the perovskite crystal quality under the cross-section, as shown in Fig. 4a–c and e–g. The thickness of the SAM layer is around 2 nm for both molecules (Fig. 4b and f), slightly higher than the molecular height estimated by theoretical calculating (Fig. S1), which suggests the formation of a monolayer covering the ITO.[22] The perovskite film, which is closer to the buried interface, shows higher crystallinity with clear lattice fringes than the perovskite part of the film at the top surface. Moreover, the perovskite at the buried interface consists of smaller grains, while the top part is formed by larger domains (Fig. S7). Both CP203 and CP204 show similar results on perovskite crystals, indicating that SAMs could affect the nucleation and growth of perovskite. However, we could observe the voids and cracks at the grain boundaries of the perovskite film deposited on CP203 (Fig. 4d). In contrast, CP204 enables a more compact perovskite

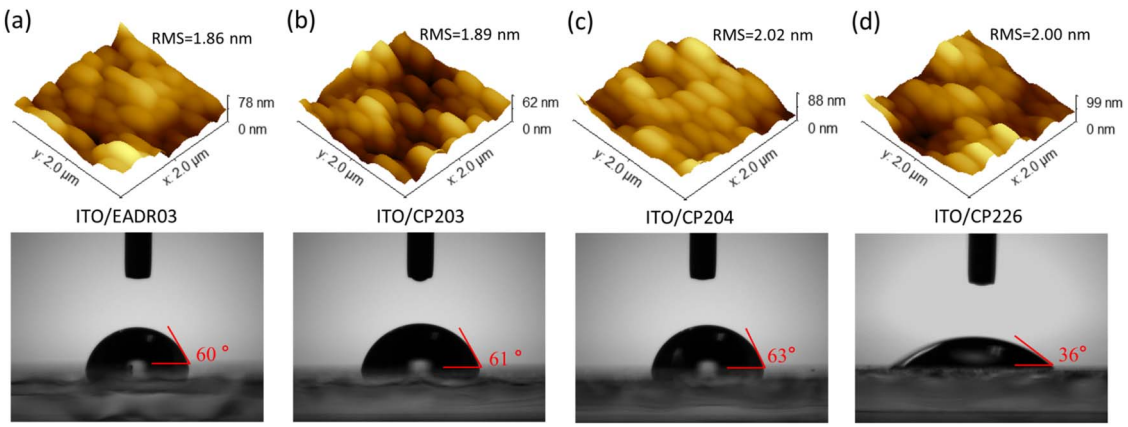

Fig. 2 AFM images and contact angles of (a) ITO/EADR03, (b) ITO/CP203, (c) ITO/CP204, (d) ITO/CP226.

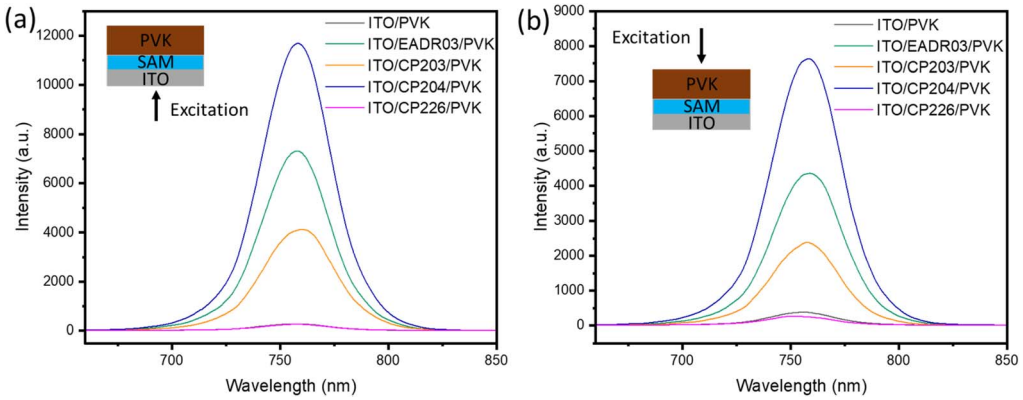

Fig. 3 Steady-state PL spectra of perovskite deposited on ITO and ITO/SAMs substrates with excitation from (a) the ITO side and (b) the perovskite side. The excitation wavelength was 635 nm.

film without obvious grain boundaries at the buried interface (Fig. 4h), which is expected to reduce the defects that act as non-radiative recombination centers at the interface. Since both SAMs have the same spacer and functional group but different anchoring groups, the difference in the morphology of perovskite films can be attributed to the ability of the anchoring groups to modulate the perovskite crystal growth. Nuclear magnetic resonance (NMR) and Fourier transform infrared spectroscopy (FTIR) measurements of mixtures of CP204 and PbI_2 at different ratios in DMF (Fig. S8 and S9) show significant peak shifts suggesting that the $-PO(OH)_2$ group can interact with PbI_2.[17,23] In contrast, the cyanoacetic acid from CP203 exhibits weak interactions with PbI_2, reflecting by small peak shifts for C≡N and C═O stretches. According to the Lewis theory of acid–base reactions, the P═O in phosphonic acid acts as Lewis's base to provide lone pair electrons, which could coordinate with PbI_2 acting as Lewis's acid, forming a coordination bond. The coordination effect could retard the perovskite crystal nucleation and crystallization, promoting the formation of high-quality perovskite film.

We further confirmed this possibility by cyclic voltammetry (CV) measurements. The surface density of molecules attached to ITO can be determined by CV using the equation below:[24]

$$i_p = \frac{n^2F^2}{4RTN_A}A\Gamma^*\nu \quad (1)$$

where i_p is the oxidative peak current, ν is the voltage scan rate, n is the number of electrons transferred, F is the Faraday constant (96 485C mol^{-1}), R is the universal gas constant (8.314 J K^{-1} mol^{-1}), T is the temperature, N_A is the Avogadro constant, A is the electrode area, and Γ^* is the surface density of molecules. The surface density of EADR03 on ITO is 3.38×10^{14} molecules cm^{-2}, while 4.29×10^{14} molecules cm^{-2} for CP203 and 3.57×10^{14} molecules cm^{-2} for CP204 (Fig. S10). However, there is no CV peak in ITO/CP226 substrate, which shows the same CV curve as bare ITO (Fig. S11). The results indicate that

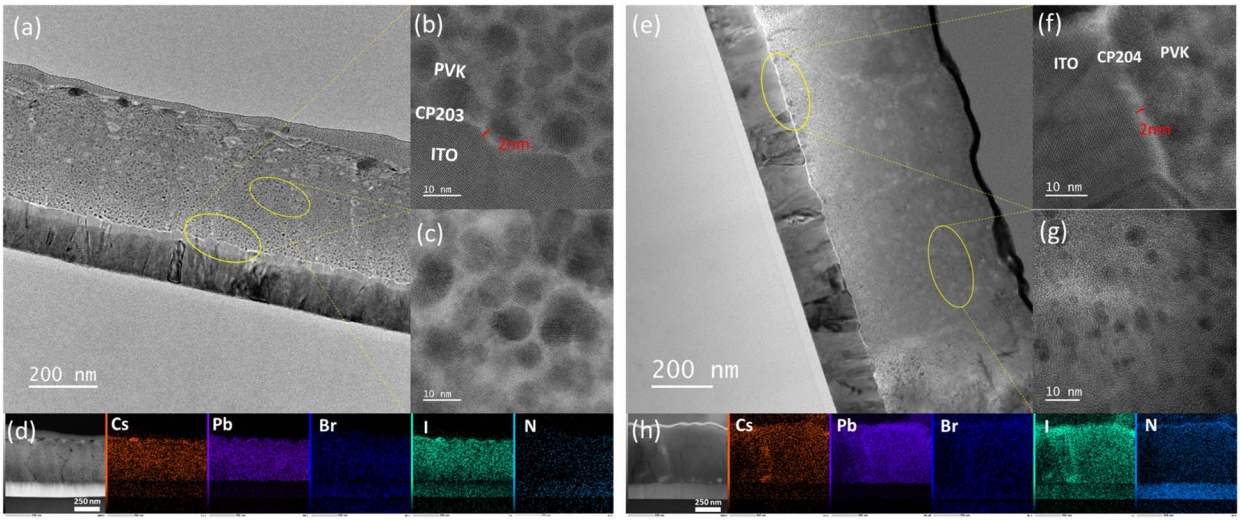

Fig. 4 High-resolution TEM image of the cross-section on ITO/CP203/perovskite (a–c) and ITO/CP204/perovskite (e–g). Cross-sectional FESEM image and the corresponding energy dispersive spectroscopy (EDS) mapping of the perovskite deposited on ITO/CP203 substrate (d) and ITO/CP204 substrate (h).

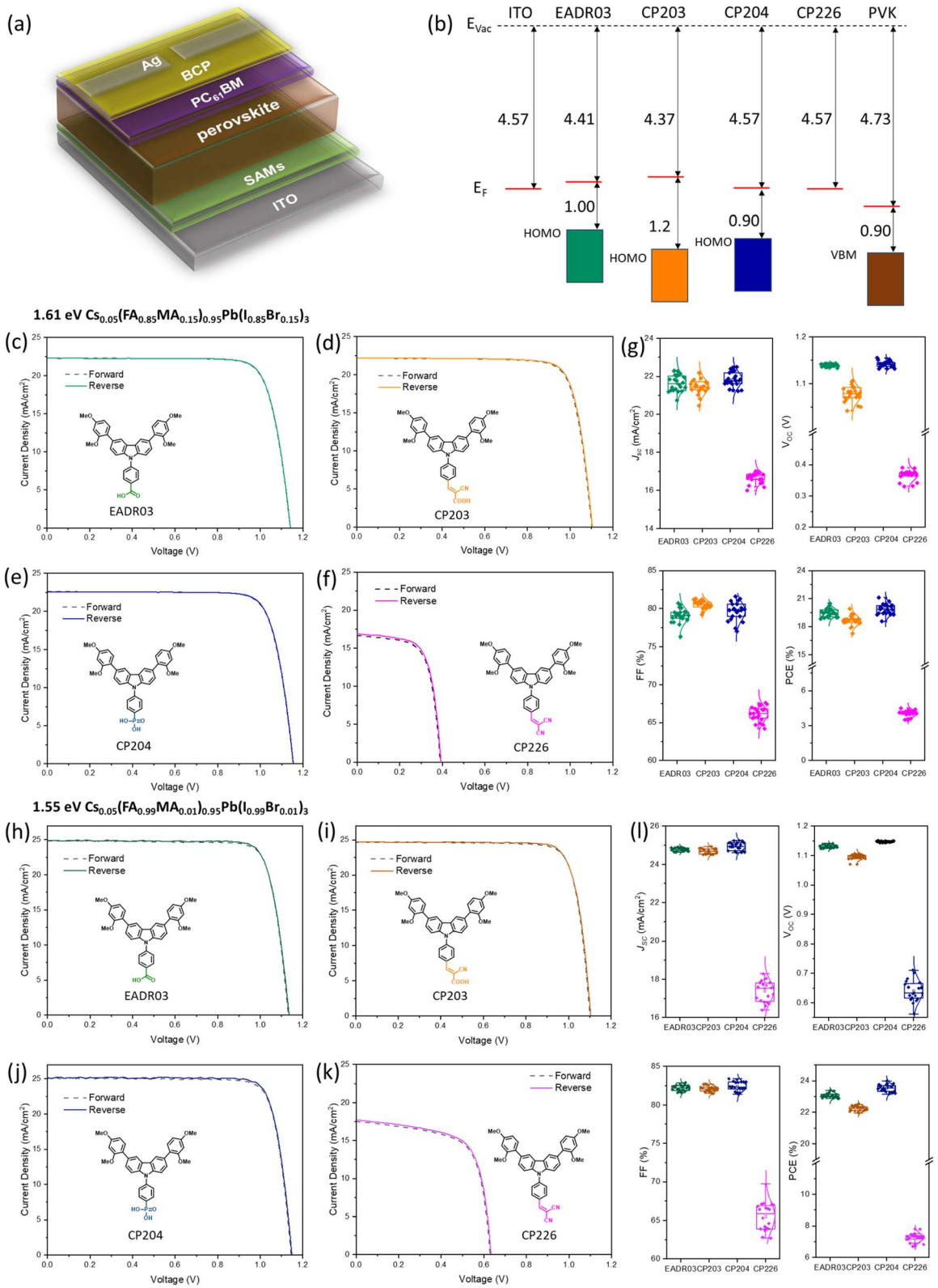

Fig. 5 (a) Schematic of the p-i-n device architecture prepared with two different perovskite compositions. (b) Schematic diagram of energy level alignment. *J*–*V* curves and statistics under simulated AM1.5G illumination of different SAM-based devices with (c–g) 1.61 eV bandgap perovskite and (h–l) 1.55 eV bandgap perovskite.

EADR03, CP203 and CP204 are deposited on the ITO surface with similar molecular density. Moreover, the multiple cycles CV measurement shows that the current in the second cycle significantly decreases compared to the first cycle and then tends to be stabilized within 5 cycles (Fig. S12). This suggests that some molecules are detached from the ITO surface after the first cycle. Thus, these unbonded molecules or anchoring groups could affect the nucleation of perovskites and the quality of thin films.

Subsequently, we performed ultra-violet photoelectron spectroscopy (UPS) on ITO/SAMs to confirm the energy levels of the molecules (Fig. S13). ITO/CP226 with CN/CN anchoring group shows the same spectroscopical features as bare ITO, indicating the ultra-low concentration of CP226 molecules on the surface of ITO. In contrast, the highest occupied molecular orbital (HOMO) levels of EADR03, CP203 and CP204 can be estimated to be 5.41 eV, 5.57 eV and 5.47 eV, respectively, as shown in Fig. 5b, which agrees well with the density functional theory (DFT) calculation (Fig. S14). Considering the valence band maximum (VBM) of perovskite with a 1.61 eV bandgap, the three SAMs show suitable energy alignment with perovskite to act as hole transport materials.

Based on the above characterizations and analysis, the SAMs with carboxylic acid and phosphonic acid anchoring groups, particularly, the phosphonic acid, are expected to have better interfacial charge extraction than the cyanoacetic acid and cyano/cyano anchoring groups. To further confirm our hypothesis, we fabricated SAM-based devices with inverted structure of ITO/SAMs/Perovskite/$PC_{61}BM$/BCP/Ag to compare the performance, as shown in Fig. 5a. The perovskite has been prepared without the use of additives to avoid bulk and surface passivation to keep the comparison as simple as possible. Fig. 5c–f show *J–V* performance of the devices under AM1.5G illumination of the best PSCs prepared with different SAMs. The corresponding photovoltaic parameters are summarized in Table 1 and S3. The CP226-based device shows low efficiency of 4.5% close to the reference device prepared without hole selective contact, as reported in our previous work.[25] The low performance of CP226 with CN/CN groups is due to the poor coverage of ITO. The EADR03, CP203 and CP204-based devices are efficient with negligible hysteresis. Specifically, the EADR03 solar cell shows efficiency of 20.5% (short-circuit current density (J_{SC}) of 22.3 mA cm^{-2}, open-circuit voltage (V_{OC}) of 1.142 V, and fill factor (FF) of 80.7%, which is similar to our previous report.[2] CP203 solar cell exhibits an efficiency of 19.9% with J_{SC} of 22.2 mA cm^{-2}, V_{OC} of 1.104 V and FF of 81.2%. In addition, the CP204 solar cell achieves the highest efficiency of 21.1% among the four SAMs, with J_{SC} of 22.5 mA cm^{-2}, V_{OC} of 1.155 V and FF of 81.0%. The boosting efficiencies from EADR03 with carboxylic acid anchoring group and CP204 with phosphonic acid anchoring group are due to the significantly increased V_{OC} when compared to CP203 with cyanoacetic acid anchoring group, as shown in Fig. 5g in the statistical distribution. Moreover, CP204 shows slightly higher J_{SC}, V_{OC} and FF than EADR03, suggesting a more effective passivation effect of phosphonic acid than carboxylic acid to minimize the interfacial non-radiative recombination. The integrated J_{SC} of the best CP204 device is 21.6 mA cm^{-2} from external quantum efficiency (EQE) (Fig. S15), consistent with the J_{SC} obtained from the *J–V* curve.

Table 1 Photovoltaic parameters of the best devices obtained under AM1.5G illumination in reverse scan direction based on different SAMs

Bandgap (eV)	SAM	J_{SC} (mA cm^{-2})	V_{OC} (V)	FF (%)	PCE (%)
1.61	EADR03	22.3	1.142	80.7	20.5
	CP203	22.2	1.104	81.2	19.9
	CP204	22.5	1.155	81.0	21.1
	CP226	16.9	0.390	67.6	4.5
1.55	EADR03	24.9	1.135	82.7	23.4
	CP203	24.7	1.103	82.6	22.5
	CP204	25.1	1.149	83.4	24.0
	CP226	17.7	0.631	67.2	7.5

Furthermore, we applied the SAMs to the 1.55 eV bandgap perovskite of $Cs_{0.05}(FA_{0.99}MA_{0.01})_{0.95}Pb(I_{0.99}Br_{0.01})_3$, which could further improve the device efficiency due to the higher current density, as shown in Fig. 5h–l and Table 1 (S4). The device performance follows the tendency of 1.61 eV-based devices. Among them, the best device from CP204 exhibits a PCE of 24.0% with J_{SC} of 25.1 mA cm^{-2} (the integrated J_{SC} from EQE is 24.8 mA cm^{-2}, Fig. S16), V_{OC} of 1.149 V and FF of 83.4%, which is comparable to the reported SAM-based PSCs incorporating bulk or surface passivation (Table S5). We also compared the device performance with and without washing after depositing the CP204 SAM layer. As shown in Fig. S17, the washed devices show a slight decrease in J_{SC}, but significant decrease in V_{OC} and FF compared to the devices without washing. The results further indicate that the unbonded molecules or anchoring groups could induce the growth of high-quality crystals and reduce the non-radiative recombination at buried interface.

Moreover, we conducted the long-term stability test with the best devices of CP203 and CP204 by maximum power point (MPP) tracking under AM1.5G illumination (Fig. S18). The device structure for the stability test is ITO/SAMs/Perovskite/$PC_{61}BM$/BCP/Ag, same as the *JV* characterizations. The encapsulated device of CP204 maintains 85% of initial PCE after 500 h MPP tracking under ambient air (40 ± 5 °C and 60 ± 5% RH), which is more stable than CP203-based device. The improved stability from CP204 arises from the high-quality perovskite film induced by the phosphonic acid groups.

We further performed the time-of-flight secondary ion mass spectrometry (TOF-SIMS) to track the ion distribution of the fresh and aged devices under one sun illumination in ambient air (40 ± 5 °C and 60 ± 5% RH) for 7 days. As shown in Fig. 6, methylammonium (MA^+) ions are depleted from the surface of perovskite films deposited on carboxylic acid and cyanoacetic acid SAMs. This decomposition facilitates Ag migration into the perovskite layer, ultimately leading to device failure. In contrast, the distributions of Ag and MA^+ ions remain largely unchanged in perovskite films deposited on CP204 SAMs. This stability is attributed to the uniform distribution of MA^+ ions throughout the film, suggesting that phosphonic acid-based SAMs promote the formation of high-quality robust perovskite layers and

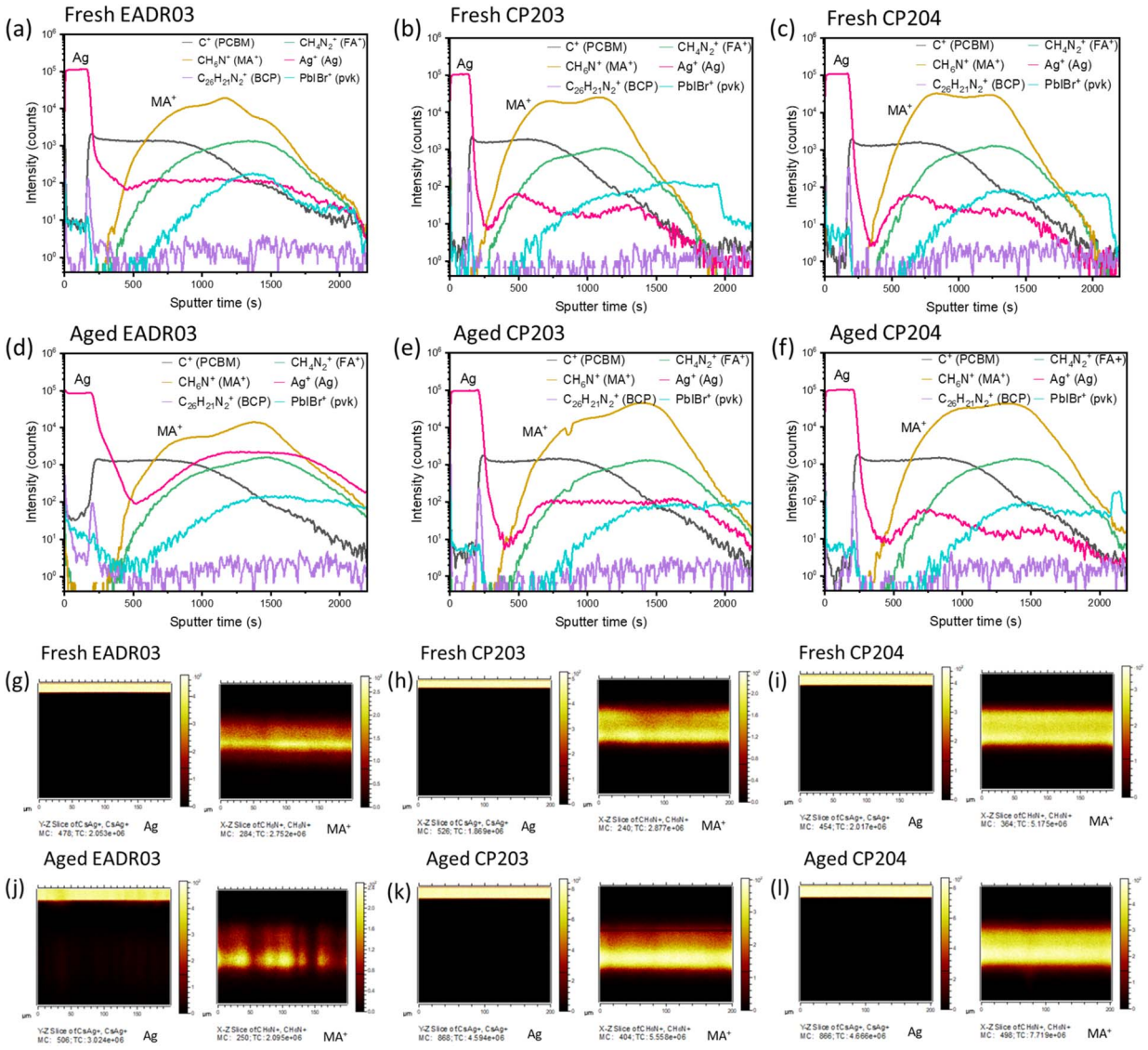

Fig. 6 The TOF-SIMS profiles of the fresh (a–c) and aged (d–f) devices with EADR03, CP203 and CP204. The cross-section of Ag and MA^+ ion distribution on fresh (g–i) and aged (g–l) devices with EADR03, CP203 and CP204.

effectively suppress degradation under external stimuli. Detailed ion distribution profiles for devices with different SAMs are provided in Fig. S19–S23.

Regarding the *J*–*V* data, and except for CP226, the main difference in the performance achieved by the devices relies on the V_{OC} value. We therefore focused on the CP203 and CP204-based devices, which significantly differ in V_{OC}, to elucidate the interfacial charge dynamics by transient optoelectronic measurements. Charge extraction (CE), transient photovoltage (TPV), and transient photocurrent (TPC), which have been well-established and reported in our previous works,[25–27] allow us to investigate the interfacial charge carrier energetics and carrier recombination kinetics under operational solar cells. In addition, differential capacitance (DC) derived from TPV and TPC can be used to estimate the capacitance (CDC) of operational solar cells and the photogenerated charge density (Q) stored in the cell at equilibrium, Q (V_{OC}), as shown in eqn (2) and (3).[28]

$$C_{DC}(V) = \frac{\Delta Q}{\Delta V} \tag{2}$$

$$Q(V_{OC}) = \int_0^{V_{OC}} C_{DC}(V)\mathrm{d}V \tag{3}$$

The DC estimates the capacitance of the electronic charge stored in the device rather than capacitance due to the redistribution of charge induced by ion migration and ion reorganization.[28] From the Q–V_{OC} data, shown in Fig. 7a, the quasi-Fermi level splitting or V_{OC} in the CP204 device is higher than that of the CP203 device under the given amount of accumulated charge in perovskite. For instance, with a similar charge density of $\sim 5 \times 10^{-9}$ C cm^{-2}, CP204 device achieves a V_{OC} of 1.1 V compared to that of 1.05 V in CP203 device, indicating that in the CP203 device there is a more significant amount of deep energetic levels in the tail states than in the devices of CP204

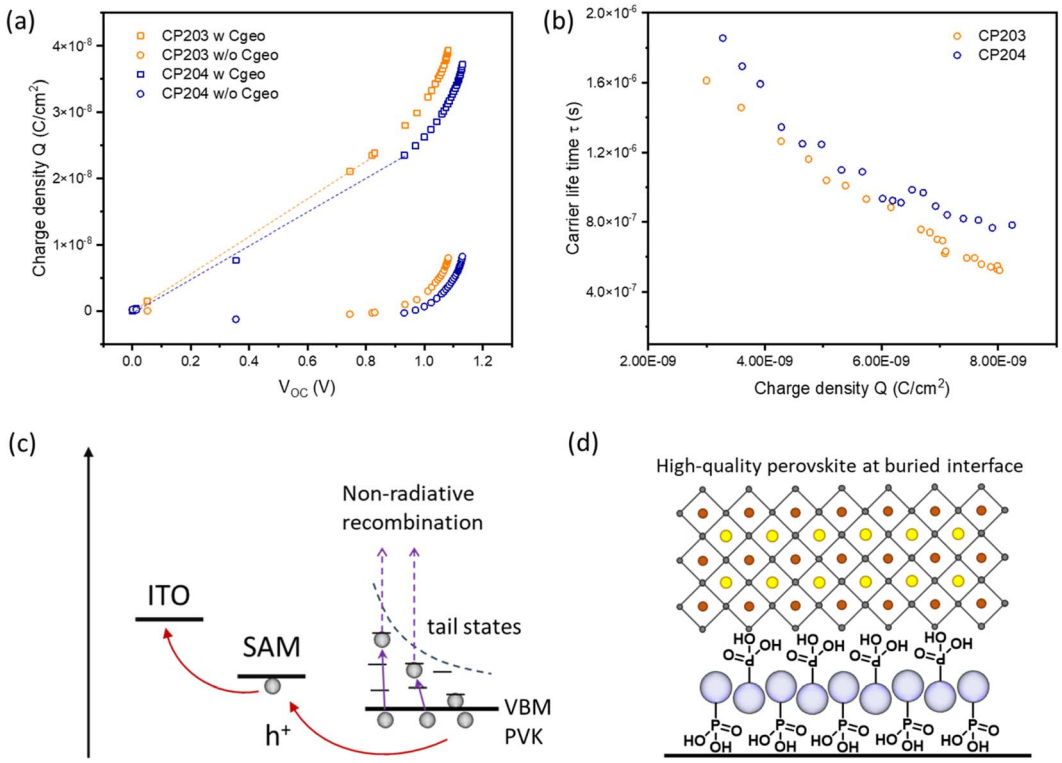

Fig. 7 (a) Charge density (Q) derived from DC in the perovskite layer as a function of V_{OC}. The dashed line represents the geometrical (C_{geo}) capacitance where charge carriers are accumulated at the ITO and Ag contacts. In contrast, the exponential part represents the chemical capacitance related to the accumulated charges in the bulk perovskite and perovskite/selective contact interfaces. The bottom curves correspond to the charge density after subtracting C_{geo}. (b) Small perturbation lifetime from TPV as a function of charge density in the devices after removing C_{geo}. (c) Schematic depiction of charge carrier recombination *via* tail states and interfacial charge transfer. (d) Schematic illustration of the anchoring groups for promoting the high crystallinity perovskite at the buried interface.

which induce the non-radiative recombination, as illustrated in Fig. 7c. The carrier lifetime derived from TPV as a function of the charge density (Fig. 7b) further confirms the charge recombination rate. For instance, with the same charge density, at $Q = 7.0 \times 10^{-9}$ C cm^{-2}, carrier lifetimes are 0.89 μs and 0.69 μs for CP204 and CP203 devices, respectively. The increased carrier lifetime indicates lower non-radiative recombination in the CP204 device compared to the CP203 device.

Combined with the PL results, the decreased concentration of tail states and non-radiative recombination of the CP204 device are related to the high-quality of perovskite deposited on the SAM with phosphonic acid anchoring group. Generally, trap states are likely to be localized at crystallite surfaces or buried interfaces and induce the non-radiative recombination, resulting in the lower V_{OC} of the device.[29–31] Thus, improving the quality of perovskite at the buried interface is essential to reduce the trap states and facilitate the charge transfer at the interface.[32] Through spin-coating process to deposit SAM, some molecules are not bonded to the ITO, instead, these molecules randomly pack on the top of the first monolayer. According to Jen's report, the SAM can be aggregated in isopropanol (IPA) solution and tend to form micelle nanoparticles.[24] Typically, the non-polar and hydrophobic carbazole-based functional groups face inwardly while the polar and hydrophilic phosphonic acids expose outwardly to form the micelles. The micelles will allow the contact of anchoring groups with perovskite solution and affect the crystal growth of perovskite, as schematically depicted in Fig. 7d. Di's report revealed that phosphonic acid groups could interact with the perovskite precursors to improve crystallinity and suppress interfacial non-radiative recombination losses, in agreement with our findings.[17] Consequently, the high-quality of the perovskite induced by phosphonic acids facilitates the interfacial charge transfer and extraction in the device which results in higher V_{OC}.

Conclusions

We have synthesized four SAMs with alike carbazole-derivatives structures but different anchoring groups, including carboxylic acid (–COOH), phosphonic acid (–PO(OH)$_2$), cyanoacetic acid (CN/COOH) and cyano/cyano (CN/CN). We have comparatively studied the effects of these anchoring groups on the ITO binding, perovskite crystal quality and interfacial charge transfer. Carboxylic acid, cyanoacetic acid and phosphonic acid anchoring groups have demonstrated a solid binding effect to the substrate. In addition, we have shown that the anchoring groups act at the buried interface, influencing the growth of the perovskite. Specifically, the CP204 SAM with phosphonic acid anchoring group promotes the development of high-quality perovskite, resulting in the best device with 24.0% PCE for 1.55 eV bandgap perovskite. The transient optoelectronic

characterizations under operational conditions reveal that the high-quality perovskite reduces the density of trap states and the interfacial non-radiative recombination, leading to a high V_{OC}. The observations made in this work contribute to elucidating the dual functions of anchoring groups of SAMs in the performance of the devices, guiding the design of molecules for breakthrough, efficient SAM-based devices.

Author contributions

Carlos E. Puerto Galvis: writing – original draft, conceptualization, methodology. José G. Sánchez: formal analysis, investigation. Eugenia Martínez-Ferrero: formal analysis, investigation, writing – review and editing. Wenhui Li: conceptualization, formal analysis, supervision, writing – original draft, writing – review and editing. Emilio Palomares: conceptualization, funding acquisition, supervision, writing – review and editing.

Conflicts of interest

There are no conflicts to declare.

Data availability

The data supporting this article have been included as part of the supplementary information (SI). Supplementary information is available. See DOI: https://doi.org/10.1039/d5el00168d.

Acknowledgements

This work is supported from Spanish Government and AGAUR (PID2022-139866NB-I00 and 2021 SGR 01261, respectively). We also acknowledge the Severo Ochoa Grant MCIN/AEI/10.13039/501100011033 (CEX2024-001469-S). C. P. and W. L. thank the support from the Horizon 2020 Marie Skłodowska-Curie COFUND grant agreement No 801474 I2: ICIQ Impulsion. This work has received funding from the European Union's Horizon Europe research and innovation programme under grant agreement No 101122283, project PEARL. E. P. also acknowledges ICIQ, CERCA, and ICREA for financial support.

References

1 S. Zhang, F. Ye, X. Wang, R. Chen, H. Zhang, L. Zhan, X. Jiang, Y. Li, X. Ji, S. Liu, M. Yu, F. Yu, Y. Zhang, R. Wu, Z. Liu, Z. Ning, D. Neher, L. Han, Y. Lin, H. Tian, W. Chen, M. Stolterfoht, L. Zhang, W.-H. Zhu and Y. Wu, *Science*, 2023, **380**, 404–409.

2 E. Aktas, N. Phung, H. Köbler, D. A. González, M. Méndez, I. Kafedjiska, S. H. Turren-Cruz, R. Wenisch, I. Lauermann, A. Abate and E. Palomares, *Energy Environ. Sci.*, 2021, **14**, 3976–3985.

3 A. Al-Ashouri, A. Magomedov, M. Roß, M. Jošt, M. Talaikis, G. Chistiakova, T. Bertram, J. A. Márquez, E. Köhnen, E. Kasparavičius, S. Levcenco, L. Gil-Escrig, C. J. Hages, R. Schlatmann, B. Rech, T. Malinauskas, T. Unold, C. A. Kaufmann, L. Korte, G. Niaura, V. Getautis and S. Albrecht, *Energy Environ. Sci.*, 2019, **12**, 3356–3369.

4 J. Du, J. Chen, B. Ouyang, A. Sun, C. Tian, R. Zhuang, C. Chen, S. Liu, Q. Chen, Z. Li, X. Wu, J. Cai, Y. Zhao, R. Li, T. Xue, T. Cen, K. Zhao and C. C. Chen, *Energy Environ. Sci.*, 2025, **18**, 3196–3210.

5 K. Zhao, Q. Liu, L. Yao, C. Değer, J. Shen, X. Zhang, P. Shi, Y. Tian, Y. Luo, J. Xu, J. Zhou, D. Jin, S. Wang, W. Fan, S. Zhang, S. Chu, X. Wang, L. Tian, R. Liu, L. Zhang, I. Yavuz, H. F. Wang, D. Yang, R. Wang and J. Xue, *Nature*, 2024, **632**, 301–306.

6 G. Qu, L. Zhang, Y. Qiao, S. Gong, Y. Ding, Y. Tao, S. Cai, X. Y. Chang, Q. Chen, P. Xie, J. Feng, C. Gao, G. Li, H. Xiao, F. Wang, H. Hu, J. Yang, S. Chen, A. K. Y. Jen, X. Chen and Z. X. Xu, *Nat. Commun.*, 2025, **16**, 86.

7 S. Wang, H. Guo and Y. Wu, *Mater. Futures*, 2023, **2**, 012105.

8 S. Y. Kim, S. J. Cho, S. E. Byeon, X. He and H. J. Yoon, *Adv. Energy Mater.*, 2020, **10**, 2002606.

9 F. Ali, C. Roldán-Carmona, M. Sohail and M. K. Nazeeruddin, *Adv. Energy Mater.*, 2020, **10**, 2002989.

10 M. Li, M. Liu, F. Qi, F. R. Lin and A. K. Y. Jen, *Chem. Rev.*, 2024, **124**(5), 2138–2204.

11 W. Li, E. Martínez-Ferrero and E. Palomares, *Mater. Chem. Front.*, 2024, **8**, 681–699.

12 S. A. Paniagua, A. J. Giordano, O. L. Smith, S. Barlow, H. Li, N. R. Armstrong, J. E. Pemberton, J. L. Brédas, D. Ginger and S. R. Marder, *Chem. Rev.*, 2016, **116**(12), 7117–7158.

13 Y. Wang, Q. Liao, J. Chen, W. Huang, X. Zhuang, Y. Tang, B. Li, X. Yao, X. Feng, X. Zhang, M. Su, Z. He, T. J. Marks, A. Facchetti and X. Guo, *J. Am. Chem. Soc.*, 2020, **142**, 16632–16643.

14 S. Zhang, R. Wu, C. Mu, Y. Wang, L. Han, Y. Wu and W. H. Zhu, *ACS Mater. Lett.*, 2022, **4**, 1976–1983.

15 Y. Luo, Y. Tian, K. Zhao, W. Mao, C. Liu, J. Shen, Z. Cheng, C. Değer, X. Miao, Z. Zhang, X. Sun, L. Yao, X. Zhang, P. Shi, D. Jin, J. Deng, M. Tian, I. Yavuz, N. Dong, R. Liu, R. Wang, D. Yang and J. Xue, *Nat. Commun.*, 2025, **16**, 4516.

16 T. Bauer, T. Schmaltz, T. Lenz, M. Halik, B. Meyer and T. Clark, *ACS Appl. Mater. Interfaces*, 2013, **5**, 6073–6080.

17 W. Xiong, C. Zou, W. Tang, S. Xing, Z. Wang, B. Zhao and D. Di, *ACS Energy Lett.*, 2023, **8**, 2897–2903.

18 C. M. Hung, C. L. Mai, C. C. Wu, B. H. Chen, C. H. Lu, C. C. Chu, M. C. Wang, S. Da Yang, H. C. Chen, C. Y. Yeh and P. T. Chou, *Angew. Chem., Int. Ed.*, 2023, **62**, e202309831.

19 W. Jiang, F. Li, M. Li, F. Qi, F. R. Lin and A. K. Y. Jen, *Angew. Chem., Int. Ed.*, 2022, **61**, e202213560.

20 P. B. Paramonov, S. A. Paniagua, P. J. Hotchkiss, S. C. Jones, N. R. Armstrong, S. R. Marder and J.-L. Brédas, *Chem. Mater.*, 2008, **20**, 5131–5133.

21 X. Zheng, Z. Li, Y. Zhang, M. Chen, T. Liu, C. Xiao, D. Gao, J. B. Patel, D. Kuciauskas, A. Magomedov, R. A. Scheidt, X. Wang, S. P. Harvey, Z. Dai, C. Zhang, D. Morales, H. Pruett, B. M. Wieliczka, A. R. Kirmani, N. P. Padture, K. R. Graham, Y. Yan, M. K. Nazeeruddin, M. D. McGehee, Z. Zhu and J. M. Luther, *Nat. Energy*, 2023, **8**, 462–472.

22 A. Magomedov, A. Al-Ashouri, E. Kasparavičius, S. Strazdaite, G. Niaura, M. Jošt, T. Malinauskas, S. Albrecht and V. Getautis, *Adv. Energy Mater.*, 2018, **8**, 1801892.
23 T. Feeney, J. Petry, A. Torche, D. Hauschild, B. Hacene, C. Wansorra, A. Diercks, M. Ernst, L. Weinhardt, C. Heske, G. Gryn'ova, U. W. Paetzold and P. Fassl, *Matter*, 2024, **7**, 2066–2090.
24 M. Liu, L. Bi, W. Jiang, Z. Zeng, S.-W. Tsang, F. R. Lin and A. K.-Y. Jen, *Adv. Mater.*, 2023, **35**, 2304415.
25 W. Li, M. Cariello, M. Méndez, G. Cooke and E. Palomares, *ACS Appl. Energy Mater.*, 2023, **6**, 1239–1247.
26 J. Jiménez-López, B. M. D. Puscher, D. M. Guldi and E. Palomares, *J. Am. Chem. Soc.*, 2020, **142**, 1236–1246.
27 C. Rodríguez-Seco, M. Méndez, C. Roldán-Carmona, R. Pudi, M. K. Nazeeruddin and E. J. Palomares, *Angew. Chem., Int. Ed.*, 2020, **59**, 5303.
28 T. Du, J. Kim, J. Ngiam, S. Xu, P. R. F. Barnes, J. R. Durrant and M. A. McLachlan, *Adv. Funct. Mater.*, 2018, **28**, 1801808.
29 X. Yang, D. Luo, Y. Xiang, L. Zhao, M. Anaya, Y. Shen, J. Wu, W. Yang, Y. H. Chiang, Y. Tu, R. Su, Q. Hu, H. Yu, G. Shao, W. Huang, T. P. Russell, Q. Gong, S. D. Stranks, W. Zhang and R. Zhu, *Adv. Mater.*, 2021, **33**, 2006435.
30 Y. Pu, H. Su, C. Liu, M. Guo, L. Liu and H. Fu, *Energies*, 2023, **16**, 5015.
31 Z. Ni, C. Bao, Y. Liu, Q. Jiang, W.-Q. Wu, S. Chen, X. Dai, B. Chen, B. Hartweg, Z. Yu, Z. Holman and J. Huang, *Science*, 2020, **367**, 1352–1358.
32 C. Bi, Q. Wang, Y. Shao, Y. Yuan, Z. Xiao and J. Huang, *Nat. Commun.*, 2015, **6**, 7747.